Comparative Thermal and Structural Characterization of Sintered Nano-Silver and High-Lead Solder Die Attachments During Power Cycling

Jingru Dai, Jianfeng Li, Pearl Agyakwa, Martin Corfield, and Christopher Mark Johnson, *Member, IEEE*

***Abstract*—13.5 mm × 13.5 mm sintered nano-silver attachments for power devices onto AlN substrates were prepared at 250 °C and a pressure of 10 MPa for 5 min and compared with Pb5Sn solder joint die attachments under constant current power cycling with an initial temperature swing of 50 °C–175 °C. Both effective thermal resistance and microstructural evolution of the samples were monitored using transient thermal impedance measurement and nondestructive X-ray computed tomography at regular power cycling intervals. The results showed a gradual increase in the effective thermal resistance of the Pb5Sn solder joints from 0.047 to 0.133 K/W from zero to 41k power cycles, followed by a rapid escalation to 0.5018 K/W at 52k cycles. This was accompanied with the formation and development of oblique cracks within the Pb5Sn die attachments until delamination occurred at the solder/device and solder/substrate interfaces. By contrast, the effective thermal resistance of the sintered Ag joints remained almost constant at 0.040 K/W up to 116k power cycles. This was explained in terms of thermally induced continuation of densification of the sintered structure and the formation and development of networked vertical cracks within the sintered Ag die attachments, some of which further extended into the Cu tracks of the AlN substrate.**

***Index Terms*—High lead solder joint, power cycling, sintered nanosilver joint, thermal impedance and microstructures.**

I. Introduction

With the increasing demand on development for more compact power modules for use under extreme temperature conditions, new technologies for higher temperature and higher density power device packaging have been under intensive investigation. High lead solder content materials such as Pb5Sn and Pb2SnAg2.5 are considered to be standard approaches for improving the reliability of solder joints for high temperature power device attachment [1], [2]. However, lead is restricted in the area of electronic assemblies due to environmental and health concerns. For high temperature lead free alternatives, Au-based eutectics (or near eutectics) and ZnAl solders are either too expensive or exhibit poor solderability [3]. Therefore, transient liquid phase bonding and/or silver sintering have been considered as attractive lead-free alternatives [4]–[6].

The sintering of micron-sized Ag particles for mounting electronic devices was first proposed by Schwarzbauer [7]. To achieve dense, highly conductive and highly reliable sintered Ag joints at temperatures below 300 °C, a quasi-hydrostatic pressure of 30 to 50 MPa was generally applied on devices to shorten the sintering process time to a few minutes [8]. A significant advance in the silver joining technology was the replacement of micron-sized Ag particles with nano-silver particles as reported in [6]–[9]. Sintered Ag joints of high quality can be obtained at temperatures below 275 °C and under pressures of a few MPa or even pressure-free [10]. Since then, research in the sintering of Ag nanoparticles for applications in power die attachment has proliferated, covering a wealth of studies including: the formulation of Ag nanoparticle pastes [11]; effects of manner and pattern of printing paste [12], [13]; sintering behaviour of silver paste [14]; metallization and surface topology of substrate on the adhesion or bonding strength [15]; large die (e.g., > 100 mm^2) attachment [16]; mechanical and thermo-mechanical properties [17], [18] to thermal cycling and power cycling reliability [19], [20].

There are numerous studies reporting the reliability of sintered Ag power die attachments subjected to thermal and power cycling tests. For example, the high reliability of small power die attachment, e.g., 1.7 mm × 1.4 mm SiC power dies on Au and Ag metallized substrates using pressure-less nano-silver sintering, was demonstrated by thermal cycling between 50 °C and 250 °C over a decade ago [10]. Similarly, no appreciable degradation was observed in the thermal impedance or cross-sections analyses of sintered Ag joints using nano-silver paste to attach 3.8 mm × 3.8 mm Si and SiC dies on direct bonded copper (DBC) substrates with bare Cu, Ni/Au and Ag finishes, after 2400 thermal cycles between −40 °C and 125 °C [19]. However, the bonding strength and bonding area of sintered Ag joints were found to degrade significantly faster than those for corresponding AuGe12

Manuscript received June 12, 2017; revised September 23, 2017 and January 3, 2018; accepted April 3, 2018. Date of publication April 12, 2018; date of current version June 5, 2018. This work was supported by the U.K. Engineering and Physical Sciences Research Council through the Centre for Power Electronics under Grant EP/K035304/1. The work of J. Dai was supported by the Mentor Graphics. *(Corresponding author: Jingru Dai.)*

The authors are with the Department of Electrical and Electronic Engineering, University of Nottingham, Nottingham NG7 2RD, U.K. (e-mail: eexjd11@exmail.nottingham.ac.uk; jianfeng.li@nottingham.ac.uk; pearl.agyakwa@nottingham.ac.uk; martin.corfield@nottingham.ac.uk; mark.johnson@nottingham.ac.uk).

Color versions of one or more of the figures in this paper are available online at http://ieeexplore.ieee.org.

Digital Object Identifier 10.1109/TDMR.2018.2825386

and Pb2SnAg2.5 solder joints attaching 2.8 mm × 2.8 mm Si and SiC power dies on bare copper substrates during a wider thermal cycling range between −65 °C and 275 °C [21].

For the reliability of large power die (> 50 mm^2) attachments, Guth *et al.* [22] reported on Ag joints attaching 16 to 185 mm^2 power dies sintered at 230 °C and 30 MPa for a few seconds to several minutes. Power cycling results between room temperature and 165 to 171 °C indicated 30 to 60 times increase in the lifetimes compared with referenced IGBT samples which were nominally assembled by a conventional solder die attachment route. Hutter *et al.* [20] studied sintered nano-silver joints to attach 9.73 mm × 10.23 mm power dies at a temperature of 230 °C and under a pressure of 30 MPa for 3 minutes. After subsequent power cycling tests between 30 °C and 180 °C, the sintered Ag joint die attachments appeared to be 10 times more reliable than corresponding Sn-Ag solder joint die attachments. Knoerr *et al.* [23] attached 50 mm^2 power diodes by using nano-silver sintering at 275 °C and 5 MPa for 60 s. Power cycling tests between 45 °C and 175 °C revealed that Si diode samples with top and bottom side nano-silver sintered joints on DBC substrates had lifetimes 17 times longer than the SnAg3Cu0.5 soldered and Al wire bonded samples.

Understanding the influence of evolving microstructural degradation on package-level reliability is of huge importance both in terms of identifying failure mechanisms and predicting lifetime. A recent study [24], reported on how the progressive reduction in attached area of substrate attach solder layer altered the junction-to-case thermal resistance under power cycling. This study, for the first time, reported on a similar non-destructive and correlative study of effective thermal impedance and microstructure for sintered nano-silver joints and Pb5Sn solder joints. The principal degradation mechanisms were identified and conclusions drawn concerning their impact on reliability and end-of-life.

The specific objectives of this paper are: (i) to compare the reliability of low pressure sintered Ag joints with high temperature Pb5Sn solder joints of a larger attach area than those reported previously in literatures; (ii) to concurrently monitor the effective thermal resistance of die attachments under power cycling and the microstructural evolution of samples characterized using non-destructive three-dimensional X-ray computed tomography; (iii) to elucidate the degradation and failure mechanisms of the sintered die attachments under power cycling.

II. Experimental Procedures

A. Materials and Sample Preparation

The power dies used were 13.5 mm × 13.5 mm × 0.5 mm, 2.5 kV, 50 A Si diodes, obtained from Dynex Semiconductor Ltd (Lincoln, U.K.). These have ∼0.1/1/1 μm thick Ti/Ni/Ag metallization on the cathode (back side) and ∼5 μm thick Al metallization on the anode (top side). The AlN-based substrates were custom manufactured from DOWA Metaltech Co., Ltd (Tokyo, Japan). Each substrate consisted of a 58.2 mm × 49.5 mm × 0.95 mm thick AlN ceramic tile with 0.25 mm and 0.26 mm thick Cu tracks actively brazed on both sides. The Pb5Sn solder alloy was a 0.1 mm thick preform, obtained from Semelab Limited, TT-Electronics (Lutterworth, U.K.). The Ag nanoparticle paste, Argomax 2020, was obtained from Alpha Assembly Solutions (Somerset, NJ 08873, USA). It was formulated with appropriate organic dispersant, binder and thinner for sintering on substrates with Ag and Au finishes. The average size of the Ag nanoparticles in the paste was ∼20 nm.

Two diodes were attached on each of the AlN-based substrates in order to achieve a layout similar to that for a conventional power module. The surface finish on the substrate for the Pb5Sn solder preform was 5 μm thick NiP followed by 0.05 μm thick Au on the top surface. For preparing the die attachment sample, two pieces of 15 mm × 15 mm × 0.1 mm Pb5Sn solder preform were placed on the substrate under the two diodes. They were put into a vacuum reflow oven preheated at 322 °C and subsequently evacuated below 5 mbar for 3 minutes, and then held at this temperature and purged with 10%$H_2$90%Ar gas (200 L/h at 1.5 bar) for 5 minutes. The reflow oven was further heated up to 350 °C and again evacuated below 5 mbar for 3 minutes. The reflow process was held at 350 °C for 5 minutes under a pure nitrogen gas flow of 200 L/h at 1.5 bar, before being cooled down to room temperature within 4 minutes.

The surface finish on the substrate onto which the Ag nanoparticle paste was applied was 5 μm thick NiP followed by 0.2 μm thick Ag-Pd on the top surface. The sintered Ag die attachments were prepared using a bespoke press. The Ag nanoparticle paste was first printed on the substrate using a 100 μm thick stainless steel stencil to form two 15 mm × 15 mm pads for the two diodes. The printed paste pads on the substrate were first dried at 130 °C for 30 minutes to evaporate the organic ingredients. In the majority of low pressure and pressure-less Ag sintering processes, power dies are placed onto pre-printed wet pastes. This practice can easily lead to poor adhesion quality of sintered joints for large area power dies owing to solvent evaporation from inner areas prior to sintering. In the present work, a type of nano-silver paste which can be pre-dried to burn out organic ingredients before die placement, was used. The two diodes then positioned centrally on the two dried paste pads on the substrate, and fixed in place with Kapton tape. The sample was turned upside down and placed on 0.5 mm thick PTFE film situated on the cold plate of the press. Final sintering was performed at a temperature of 250 °C and a pressure of 10 MPa for 5 minutes before releasing the pressure and cooling the sample down to room temperature within 3 minutes. These sintering parameters were selected to ensure a bonding strength of above 40 MPa, based on previous process optimization for the same Ag nanoparticle paste [25].

Only one diode on each substrate was tested during the power cycling test. After attaching the diodes, ultrasonically bonded Al wires were used to establish the interconnections between the tested Si diode and the Cu tracks on the substrate. Al wires with a diameter of 375 μm were adopted and ten stitch bonds were made for each sample. When/if Al wire lift-off occurred during the power cycling tests, new bonds were made to replace the failed bonds. In addition, bus bars made of

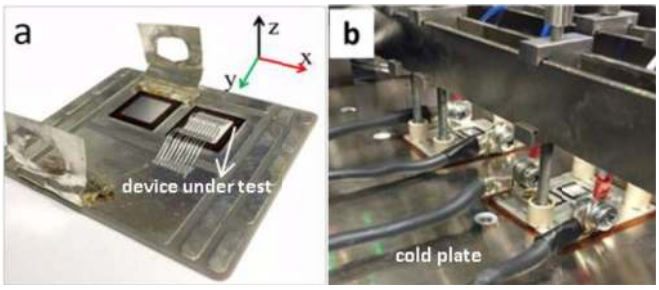

Fig. 1. Images of one as-assembled sample (a) and two samples mounted on the cold plate of the power tester (b).

0.125 μm-thick Ag foil were soldered onto the substrate with Sn36Pb2Ag solder paste at a peak temperature of 200 °C.

B. Power Cycling and Transient Thermal Tests

Both power cycling and transient thermal tests were carried out using a Mentor Graphics 1500A Power tester platform. Fig. 1 shows images for one as-assembled sample and two samples mounted onto the cold plate of the power tester rig. Two layers of 25 μm-thick Kapton film were placed under each of the samples to increase the thermal resistance between the substrate and the cold plate in order to achieve the desired temperature swing. The cold plate was kept at a constant temperature of approximately 20 °C by a recirculating chiller.

During tests the samples were power cycled using a constant current mode with a current of around 82 A. The heating (current) on time and off time were fixed at 13 s and 5 s respectively, making an initial temperature swing between 50°C and 175 °C for both samples. The junction temperature T_j of the Si diode on each sample was monitored by the forward voltage drop V_F across the diode by passing through a measurement current of 200 mA. A calibrated curve of $T_j = f(V_F)$ was derived from the V_F values measured under the measurement current of 200 mA at several fixed temperatures ranging from 20 °C to 70 °C prior to power cycling.

The transient thermal tests for measuring the thermal impedance curves were conducted in-situ prior to power cycling and intermittingly (when the power cycling test was paused) after every 1000 cycles. During each measurement, a heating current of 55 A passed through the diode for 60 seconds to reach thermal equilibrium. The heating current was switched off and the voltage drop across the diode (under the measurement current) was recorded. Using the relationship between T_j and V_F, the recorded data of the forward voltage was converted to the junction temperature of the diode during the cooling stage. The resulting transient thermal impedance was determined from the step-response as follows:

$$Zth(t) = \frac{T_j(t_0) - T_j(t)}{P} \tag{1}$$

where Zth is the transient thermal impedance, $T_j(t_0)$ is the junction temperature at the end of the heating stage, $T_j(t)$ is the junction temperature at time t during the cooling stage, and P is the dissipated power. It should be noted that voltage data from the very early cooling stage (i.e., before a transient cooling time of 1.0^{-3} s) was not included when determining the thermal impedance curves owing to the presence of switching noise.

From the experimental measurement of the thermal impedance, the heat-flow path can be modeled by a high order Cauer network with a series of pairs of thermal resistances (R) and capacitances (C) [26]. By means of an evaluation tool named 'T3Ster-Master' which is integrated to the power tester, the RC network model is produced to obtain a structure function capable of identifying the heat conducting structure in the sample by separating the key elements of the heat-flow path from the diode to the heatsink. The cumulative structure function represents the cumulative thermal capacitance $C_\sum$ as a function of cumulative thermal resistance $R_\sum$. The differential structure function $K_\sum$ represents the derivative of the cumulative capacitance $C_\sum$ as a function of the cumulative thermal resistance $R_\sum$, as expressed by the following relationship [27]:

$$K_\sum = \frac{dC_\sum}{dR_\sum} = \lambda C A^2 \tag{2}$$

where A is the cross-sectional area of heat-flow path, C is the thermal capacitance and λ is the thermal conductivity of the material. Thus, in a differential structure function plot of $K_\sum$ versus $R_\sum$, a peak corresponds to an interface between two materials, and the "distance" between two adjacent peaks on the x-axis represents the thermal impedance/resistance of the material. Note that this interpretation of the differential structure function is strictly only valid for one-dimensional heat flow, so in the following we refer to this "distance" as an effective thermal resistance.

C. Microstructure Characterization

Microstructural development of the die attachment at different stages of power cycling was characterized by non-destructive 3D X-ray computed tomography (CT) imaging carried out on a Zeiss Xradia Versa XRM-500 CT system. This was conducted on as-assembled samples and approximately after every 5k power cycles, or when the effective thermal resistance of the die attachment layer appeared to increase significantly. A source voltage of 160 kV was used and a 0.4 X objective detector was applied for acquisition. An appropriate filter was selected to minimize artefacts such as beam hardening. These setup parameters enabled a spatial resolution of around 6.6 μm which allowed observation of the formation and development of cracks and voids.

The porosity, referred to as "true" porosity, of the as-sintered Ag joint was determined by measuring the weight and volume of the sintered Ag joint as the method reported previously in [14]. The weight measurement of the sintered Ag joint was conducted by transferring the same amount of printed and dried Ag paste onto 13.5 mm × 13.5 mm Si diodes and then weighing them using a highly accurate digital balance with a resolution of 0.0001 g. The volume of the sintered Ag joint was calculated from its thickness which was measured using both optical profilometry and scanning electron microscopy (SEM) image analysis methods.

SEM images and elemental analysis/distributions of both as-prepared samples (prior to power cycling test) and samples after power cycling were taken using a Hitachi TM3000 desktop Scanning Electronic Microscope (SEM, Hitachi High-Tech, Minato-ku, Tokyo 105-8717, Japan) and Quantax 70 energy-dispersive X-ray spectroscopy (EDXS) microanalysis system. For the SEM observation and imaging, all the samples were cross-sectioned, ground with SiC abrasive papers and then polished with diamond slurries. For thickness measurement of the as-sintered Ag joint, 10 SEM images (1280 × 960 pixels) which were evenly distributed along the 13.5 mm cross-sectional length of the polished sample were taken. The "apparent" porosity of the as-sintered Ag joint was also measured from 3 typical SEM images by the image analysis method given in [25]. The "apparent" porosities, i.e., the percentages of voids plus cracks within both the solder and sintered joints were also estimated (using the image analysis method) from the virtual X-ray CT slices of the die attachment layer parallel to the X-Y plane (in the plane of the bond-line as indicated in Fig. 1(a)).

III. Results

A. Thermal Performance During Power Cycling Test

As shown in Fig. 2, the differential structure functions obtained from the samples reveal a series of peaks, each one associated with an interface between adjacent layers in the thermal path. It is thus possible to obtain estimates for the effective thermal resistances of the die attachment layer, upper copper layer, AlN ceramic title, lower copper layer, Kapton film and heatsink to ambient. Note that temperature data from the first 10^{-3} s of the transient are ignored, owing to the presence of switching noise and thus there is no information about the contribution of the diode itself to the overall thermal impedance. In contrast, the two peaks of the die attachment layers can readily be identified and any changes with increasing power cycles resolved. Changes in amplitude and shift in the peaks relating to the other material layers become increasingly difficult to identify with increasing distance from the diode die. This is compounded by variability in the thermal contact between the Kapton film and the heatsink because of repeated unmounting and re-mounting (the sample was taken off from the power tester for imaging and then re-mounted afterwards leading to a change in thermal contact between the Kapton film and the heatsink). Therefore, it is not possible to isolate the die attach thermal resistance from the observed changes in overall thermal resistance and so the effective thermal resistance obtained from the differential structure function is used to overcome this limitation.

As can be seen from Fig. 2(a), with increasing power cycles, the predominant peak for the Pb5Sn die attachment layer shifts gradually over the x-axis to the right, indicating a progressive increase in the thermal impedance/resistance of the soldered joint. There is also a significant reduction in amplitude for the die attachment peak, implying a reduction in conducting area of the Pb5Sn solder joint die attachment layer, as given by (2). In contrast, it is difficult to see any appreciable change in the peaks in the sintered Ag joint die attachment as shown in Fig. 2(b) indicating a virtually constant effective thermal resistance throughout the test.

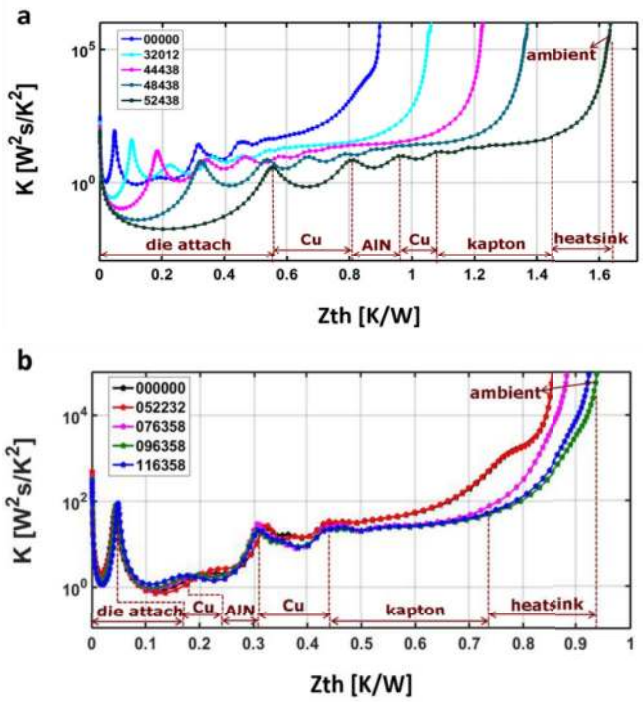

Fig. 2. Representative differential structure functions obtained during the power cycling tests from the diode samples with: (a) Pb5Sn solder joint die attachment; (b) sintered Ag joint die attachment.

The effective thermal resistance values of the die attachment layers were extracted from the differential structure functions by measuring the distance/values between the two peaks of the die attachment layer. Fig. 3 presents the extracted thermal resistance values of both samples during the power cycling test, where the error of the extracted resistance values was estimated to be ± 0.0044 K/W. The effective thermal resistance of the Pb5Sn solder joint die attachment was evaluated to be 0.0467 K/W prior to power cycling. A gradual increase to 0.1334 K/W (an increase of 186 %) was observed after 41k power cycles, and then a dramatic increase leading to the termination of the power cycling test after 52k cycles. In actual fact, a 20 % rise in thermal resistance of the Pb5Sn solder die attachment occurred after only 11k cycles.

The effective thermal resistance value of the sintered Ag joint die attachment remains relatively constant at 0.04 ± 0.004 W/K up to 80k cycles, with only nominal increases observed after this point. The power cycling test was terminated after 116k cycles when cracks in the sintered Ag layer, observed from the reconstructed X-ray CT images, were seen to extend into the upper Cu layers of the substrate, as detailed below.

B. Microstructures of the As-Prepared Joints

As can be seen from Fig. 4, there is a thin layer of Ni-Sn intermetallic compound (IMC) formed at the interfaces between the Pb5Sn solder and both the Ni finish on the Si diode and the NiP finish on the AlN-based substrate in the as-reflowed Pb5Sn solder joint die attachment. This gives

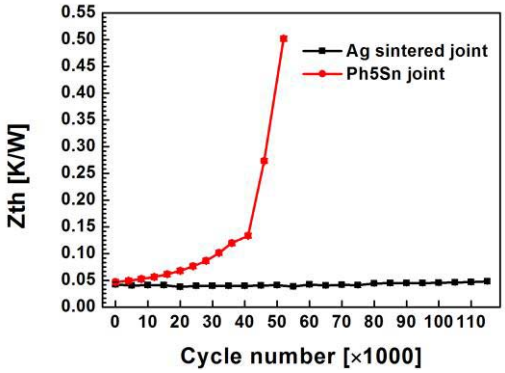

Fig. 3. Evolution of thermal resistance values of die attachment layers in soldered specimen (a) and sintered sample (b) during power cycling test.

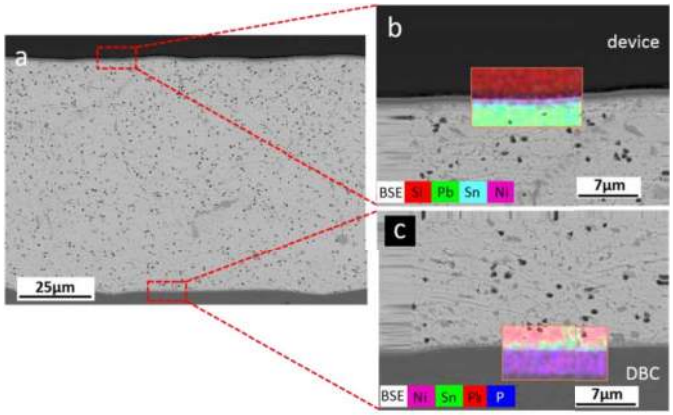

Fig. 4. SEM images taken from the polished cross section of one as-reflowed Pb5Sn solder joint (b and c are enlarged view of the boxed areas in a).

an indication of good metallurgical bonding formed at the interfaces (although the layer of IMC was too thin to determine its exact composition). In addition, the ∼1 µm Ag finish on the as-received Si diode and ∼0.05 µm Au finish on the as received substrate appear to have dissolved into the molten solder during the early reflow stage, though it is difficult to detect any Ag and Au in the as-reflowed solder joint. The thickness of the solder joint was ∼79.1 µm.

As can also be seen from Fig. 5, a uniform microstructure and good adhesion on both the Si diode and AlN-based substrate were achieved for the as-sintered Ag joint. The average thickness of the as-sintered Ag joint was estimated to be ∼ 27.8 µm. The visible voids/pore distribution in these SEM images ranged between 73 nm to 753 nm in diameter, and the "apparent" porosity measured by analyzing the SEM images was 2.4 %. By contrast, the "true" porosity determined by measuring the weight and volume was 18 %. Therefore, the majority of the voids/pores in the as-sintered Ag joint are deemed smaller than 73 nm in size and thus are unable to be resolved from the SEM images.

C. Progressive Microstructure Characterization During Power Cycling

From the reconstructed X-ray CT images shown in Fig. 6, the majority of measured voids/pores are within a 0.2 mm to

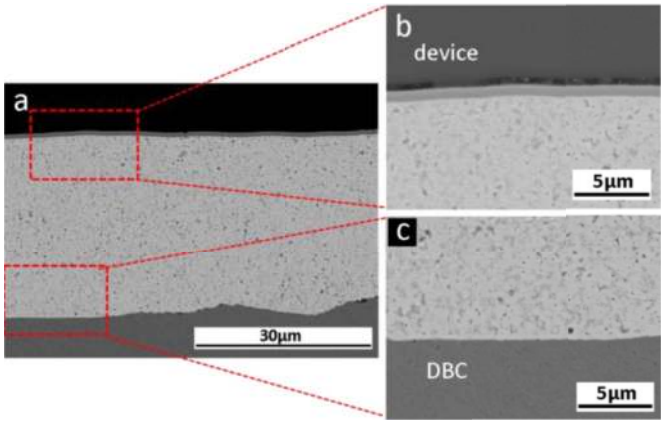

Fig. 5. SEM images taken from the polished cross section of the as-sintered Ag joint.

1 mm range in the Pb5Sn solder joint during the early stages of power cycling. However, the formation and growth of the cracks during cycling does not necessarily appear related to these defects, but rather they are initiated from the whole area of the solder layer and they appear more frequently at the center region than the edges. After 52k powercycles, the cracks are well developed and interconnected into a networked structure. Fig. 7 shows a virtual X-ray tomography X-Z cross-sectional image with higher magnification. The networked cracks are inversed 'V' cracks to the through thickness direction, and extend somewhat into both the solder/Si and solder/substrate interfaces after 52,438 power cycles.

Fig. 8 shows the measured "apparent" porosity for a Pb5Sn solder layer as a function of number of power cycles. The porosity increases nearly linearly from 9.7 % to 32.2 % with increasing power cycles up to 41k. At the initial stage, the rise in the "apparent" porosity may be ascribed to the increase in the number of pores, voids and cracks, as seen in Fig. 6(a)/(b). After about 41k power cycles, the "apparent" porosity seems to increase at a reduced growth rate, and reaches 35 % after 52k power cycles with cracks well developed and interconnected into a networked structure. The reduction in the growth rate may be related to the maturity of the oblique cracks within the Pb5Sn layer and their subsequent extension into the solder/device and solder/substrate interfaces. The interfacial delamination causes a dramatic increase in the thermal resistance of the soldered die attachment joint as shown in Fig. 3.

Figs. 9 and 10 are representative reconstructed X-ray CT images obtained for sintered Ag die attachment. The formation and growth of crack networks is most prevalent in the central regions of the sintered die attachment joint. However, these networked cracks are narrower (9.1-45.3 µm) than those in the solder joint (27.2-77.1 µm) and almost perpendicular to the die attachment interfaces (parallel to the through-thickness direction). Furthermore, there are localized areas which are clearly brighter than the surrounding areas in the images which increase with increasing power cycles. The appearance of these brighter localized areas results from variable attenuation of the X-rays, and hence indicates denser Ag regions in the samples. In addition, vertical cracks are seen to extend into the upper

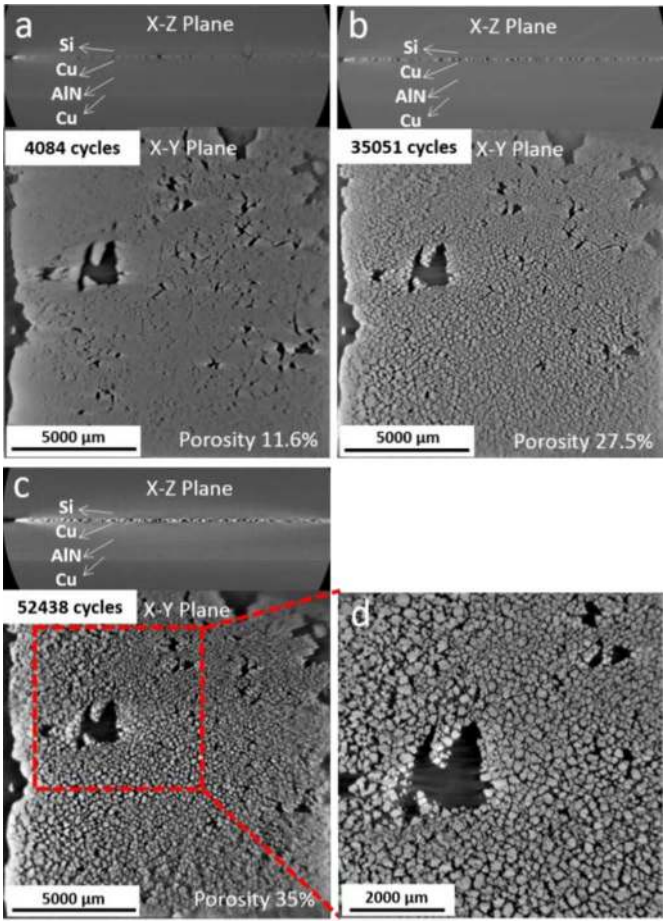

Fig. 6. Virtual X-ray tomography cross-sectional images showing progressive microstructures of Pb5Sn solder joint die attachment under power cycling (d is the enlarged view of the area boxed by the red lines in c).

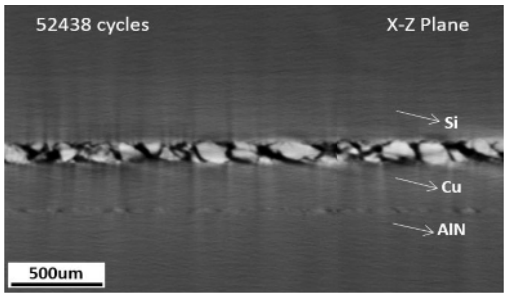

Fig. 7. Virtual X-ray tomography X-Z cross-sectional image with higher magnification, showing reverse 'V' shape cracks and significant interfacial delamination.

copper layer of the AlN-based substrate in the sintered sample after 116k power cycles (Fig. 10).

Fig. 11 shows the measured "apparent" porosity of the sintered Ag joint die attachment as a function of number of power cycles. The "apparent" porosity increased at a variable growth rate from 0.6 % at zero cycle to 13.6 % at 116,358 power cycles. The increase in the "apparent" porosity can be attributed to the increase in the number, length and width of the vertical cracks formed during power cycling.

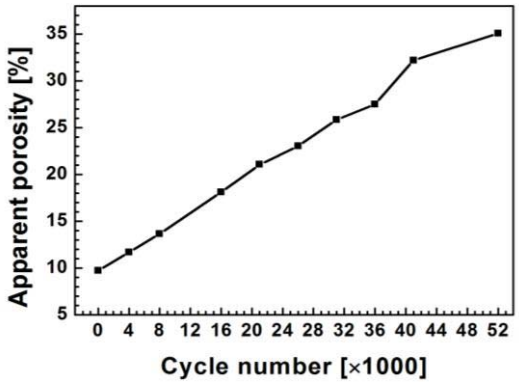

Fig. 8. Evolution of "apparent" porosity of the Pb5Sn joint die attachment layer obtained from the virtual X-ray tomography X-Y cross-sectional images, during the power cycling test.

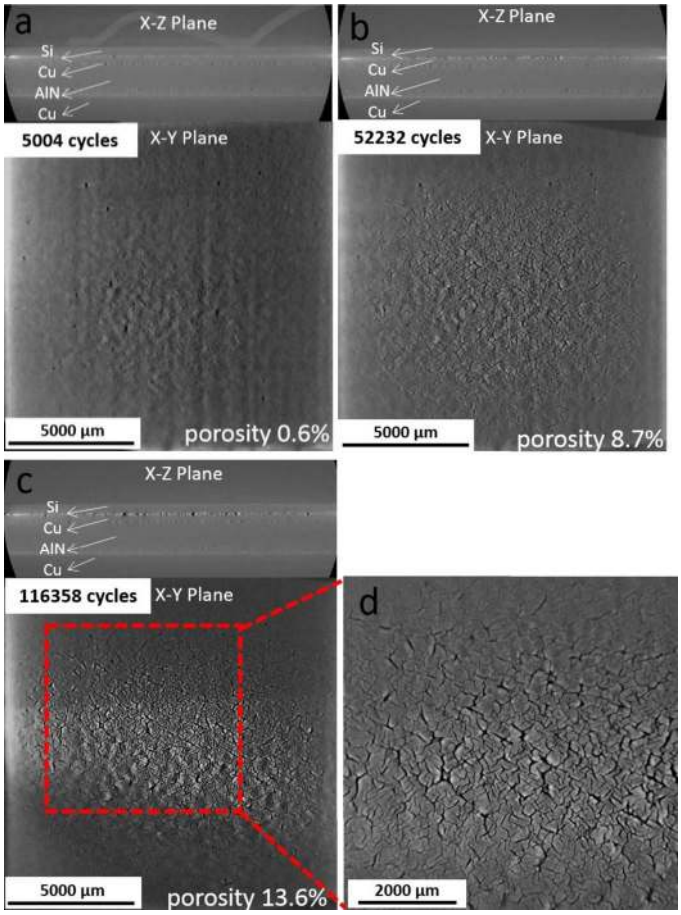

Fig. 9. Virtual X-ray tomography cross-sectional images of the sintered Ag joint die attachment showing evolutional microstructures under power cycling (d is the enlarged view of the area boxed by the red lines in c).

D. Microstructures After the Power Cycling Test

From the SEM images in Fig. 12, it can clearly be seen that the oblique cracks are along the grain boundaries in the Pb5Sn solder joint die attachment after power cycling test (Fig. 12(a), (c) and (d)). These were merged as inverted "V" shape cracks near the solder/die interface, and further extended as interfacial cracks at the solder/Ni-Sn IMC interface at the substrate side.

From the SEM images shown in Fig. 13, it can be seen that the majority of the vertical cracks with widths of 0.29 µm

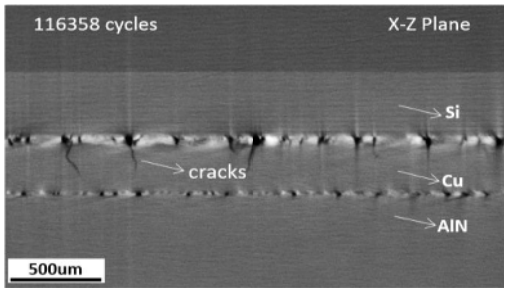

Fig. 10. Virtual X-ray tomography X-Z cross-sectional image with higher magnification showing cracks extending into Cu layer.

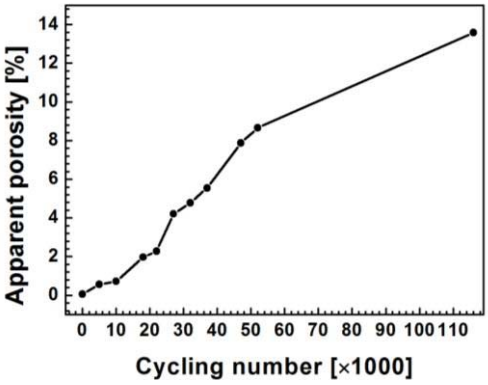

Fig. 11. Evolution of the "apparent" porosity of the sintered Ag layer obtained from virtual X-ray tomography X-Y cross-sectional images during the power cycling test.

to 51.8 μm have penetrated through, but still limited within the sintered Ag layer, after the power cycling test. Because the cracks are predominantly vertically orientated, they result in a negligible amount of interfacial discontinuity. With the exception of locations where vertical cracks come into contact with the die or with the substrate, there is still good adhesion at both the Ag/die and the Ag/substrate interfaces. A few cracks have extended into the Cu layer, as shown in Fig. 13(b). No such cracks were found in the Pb5Sn solder joint die attachment after power cycling. The cracks, extending into the Cu layer, are much wider in the Ag layer than in the Cu layer.

High magnification SEM images similar to that seen in Fig. 13(c) show grains of ∼10 μm in size clearly visible in the majority of the cross-sectional area of the sintered Ag layer, and all the voids/pores localized at grain boundaries after power cycling. These voids/pores are measured between 0.3 μm and 6.7 μm. Excluding the vertical cracks, the localized "apparent" porosity is in the range of 0 to 14.3 % (a mean of ∼ 7 %). With the visible Ag grains in the SEM images the determined "apparent" porosity values should reflect and be representative of the "true" porosity values of the different cross-sectional areas of the sintered Ag layer after the power cycling test.

IV. Discussion

A. Reliability Comparison of the Die Attachments

The power cycling reliability of sintered Ag to attach large power dies (> 50 mm^2) [14], [20], [22], [28], has mainly been

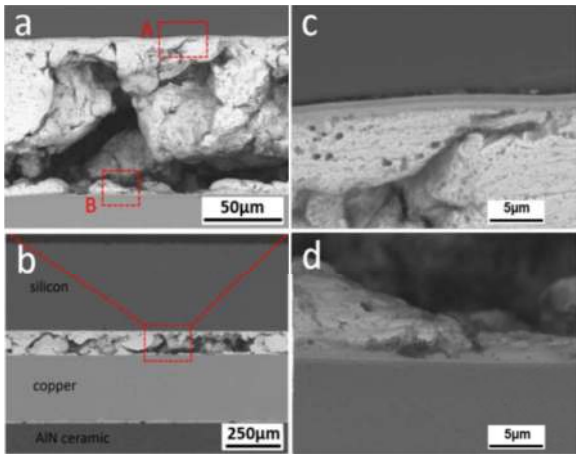

Fig. 12. SEM images of the Pb5Sn solder joint die attachment after 52,438 power cycles (a is the enlarged view of the area boxed by the red lines in b, c and d are the enlarged view of area A and B in image a).

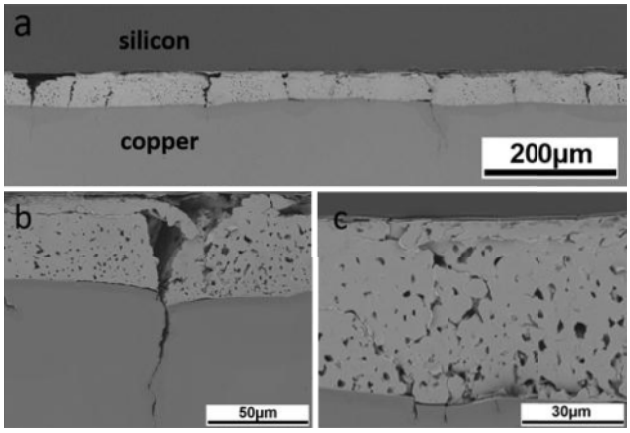

Fig. 13. SEM images of the sintered Ag joint die attachment after 116,358 power cycles.

compared with eutectic or near eutectic SnAg and SnAgCu solder joints based on Au and/or Ag finish substrates. Due to the high melting point of pure Ag (about 960 °C), sintered Ag joints have relatively high creep resistance and are hence more reliable under power cycling tests with peak temperatures of 165 °C to 180 °C. This can readily be understood as Sn-based solder joints are prone to creep at temperatures above 125 °C and the accumulation of plastic work leads to crack initiation and propagation [1].

In a study [21] comparing sintered Ag joints with AuGe12 and Pb2SnAg2.5 solder joints to attach 2.8 mm × 2.8 mm Si and SiC power dies on bare copper substrate under thermal cycling tests, the sintered joints degraded significantly faster than the solder joints. One possible reason is that the oxygen trapped in the interconnected pores/voids within the Ag layer during the sintering process might have caused copper oxide at the interface between the sinter layer and the bare copper substrate weakening the bond during cycling. In the present work, the 5/0.2 μm thick Ni-P/Ag-Pd finish on the Cu-AlN-Cu substrate provides sufficient protection against oxidation despite the fact that the sintered Ag joint has a "true" porosity of around 18 %. Dies of the same size are considered under the

same power cycling conditions. Under these test conditions the lifetime of sintered Ag joint is at least 10 times greater than that of high lead Pb5Sn solder joint (where an increase of 20 % in the thermal resistance is employed as the criterion of failure).

B. Evolution of Thermal Resistance During Power Cycling

The present results extracted the thermal resistance contribution from the die attachment layers only, and compares nano-silver sintered die attachment with high temperature high lead Pb5Sn die attachment. Similar to the evolution of the thermal resistance of samples with eutectic Sn3.5Ag solder die attachments [29], the thermal resistance of the present Pb5Sn solder die attachment increased gradually until around 186 % with cycles reaching 41k. Therefore, an increase of 20 % in the effective thermal resistance is taken as the failure criterion for thermal design, this value does not reflect any dramatic changes in the thermal performance of the die attachment itself. With the consideration of measurement error, the present nano-silver sintered die attachment exhibits a stable effective thermal resistance of 0.04 $\pm$ 0.004 K/W up to 116k power cycles under an original delta T of 125 K, as is similar to the stability of the thermal resistance of a high pressure micro-silver sintered sample during 90k power cycles between 40°C and 128 °C [30].

C. Evolution of Microstructure During Power Cycling Tests

In the present work, the progressive microstructures of samples during power cycling tests were observed with non-destructive X-ray CT images. The initiation and growth of cracks in the Pb5Sn soldered samples start from the whole area but more extensive in the center regions, whereas that in the nano-silver sintered samples start from the interior regions of sintered die attachment layer. The vertical cracks (perpendicular to the die attachment layer) form in the nano-silver sintered die attachment layer were seen to extend into the upper Cu layer of the AlN-based substrate. The initiation and growth of the cracks from the interior regions of the sintered die attachment layer can readily be understood because the most extreme thermal excursions occur directly under the centre of the die during the power cycling tests where more densification happens. Similarly, more crack development occur in the central regions although crack initiation sites are usually near the Sn rich areas in the Pb-Sn soldered joints [31]. The present results reveal different microstructures in the two types of samples. A more complete description of the crack formation in the samples can be better explained, and correlated, with the measured thermal resistances as detailed below.

In the as-reflowed Pb5Sn soldered joint formed through melting and resolidification of solder, the origins of these cracks are considered to be related to a typical microstructure morphology of grain boundary-sliding induced creep cracks which were clearly demonstrated in the SEM images (Fig. 12). During power cycling, the thermo-mechanical stress caused by the mismatch of coefficient of thermal expansion (CTE) between the die attachment layer and the die and substrate can lead to creep strain/work accumulation and crack initiation and propagation at these grain boundaries. Once these oblique cracks were merged as inverted "V" shape cracks near the solder/Si interface, they further extended into interfacial cracks at the solder/Ni-Sn IMC interface at the substrate side, resulting in rapid failure as the maximum junction temperature had increased to 237 °C from 175 °C under the constant current power cycling mode.

The regular and networked vertical cracks in the nano-silver sintered die attachment can be ascribed to further densification and development of tensile stress and strain within the sintered Ag layer. It is speculated that the inter-diffusion of silver for densification is mainly responsible for the formation and development of vertical cracks which could be regarded as "super pores" after densification. This is because the mechanical stress resulted from less than 15 ppm mismatch of coefficient thermal expansion between the Si chip and substrate should be much lower than the stresses caused by silver densification with a reduction in the porosity of $\sim$ 10 %. The overall morphology and mechanism of these cracks may be analogous to those of mud cracks formed as muddy sediment dries and contracts. The $\sim$ 10 μm Ag grains after power cycling were significantly larger than those ($<$100 nm) in the as-sintered condition, and the growth of grains is in general accompanied by further densification. The mean $\sim$7 % apparent" porosity" of the sample after the power cycling test (excluding vertical cracks) was lower than the "true" porosity of 18 % for the as-sintered sample. Increasingly dense local areas, close to the more developed cracks during the power cycling test, were observed by X-ray CT images. Further densification caused the contraction (significantly higher than the corresponding thermal expansion/contraction) where tensile stress and strain were developed within the sintered die attachment layer because both the die and substrate constrained such contraction. The vertical cracks were then formed and propagated once the development of the tensile stress and strain reached a critical value. These are well supported by the continued microstructure observation by non-destructive X-ray CT, which were not revealed in the previous work on the power cycling reliability of the either the micro-scaled Ag or nanosilver sintered die attachments [20], [23].

The cracks extending into the Cu layers of the substrates were regarded as a main failure mode in both the nano-silver and micro-silver sintered die attachment samples during power cycling tests [20], [28]. In the previous work [20], the upper copper of the substrate was considered to fail first due to mechanical stress, which then caused interfacial cracks and delamination near the sintered die attach layer. In [32] the cracks were assumed to start from the interface between the sinter silver and the top side Cu layer of the substrate, and then extend into both the sintered Ag layer and the copper layer due to mechanical load. However, the present results do not fully support either of these two explanations. This is because in the present work only some vertical cracks within the sintered die attachment layer penetrate into the copper layer. Moreover, the widths of the cracks in the sintered die attachment layer are wider than those which extend into the copper layer. In particular, the X-ray CT images revealed that it was only during the

later stages of power cycling that the cracks extended into the top-side Cu layer of the substrate, whereas during the early stages they were formed and propagated within the sintered die attachment layer only. The extension of cracks into the copper layer is more probably related to further densification of silver leading to the formation and growth of vertical cracks within the sintered die attachment layer. This is because the well-developed vertical cracks within the sintered die attachment layer would lead to high local tensile stress and strain under the formed vertical cracks.

D. Correlation of Effective Thermal Resistance With Microstructure

During the power cycling test from 0 to 41k cycles, both the effective thermal resistance (Fig. 3(a)) and the "apparent" porosity (Fig. 8) of the Pb5Sn soldered gradually increased with an increase in the number of power cycles, but the growth rate of the effective thermal resistance was speculated to be 1.6 to 7.7 times higher than that observed for the "apparent" porosity. Because the formation and growth of the oblique cracks, leading to a reduction in the total effective cross-sectional area of the heat flow path passing through the die attachment layer, as opposed to an increase in the percentage (by volume) of the cracks and pores in the die attachment layer. After 41k cycles, the oblique cracks were fully developed and merged as inverted "V" shape cracks near the solder/Si and solder/substrate interfaces. The subsequent development of the interfacial cracks caused a more significant reduction in the effective cross-sectional area of the heat flow path passing through the die attachment layer. Therefore, the effective thermal resistance increased dramatically and the die attachment failed rapidly.

During power cycling, further densification of the sintered die attachment with initial "true" porosity of 18 % would reduce the effective thermal resistance. On the other hand, the formation and growth of the vertical cracks would effectively increase the effective thermal resistance because of a reduction in the effective cross-sectional area of the heat flow path. Thus, these competing processes act in tandem to result in a relatively constant effective thermal resistance value of 0.04 ± 0.004 W/K before 80 k cycles. The slight increase in thermal resistance after 80 k cycles may be caused by delamination of Ag from the Si die occurring locally in the vicinity of the relatively wide cracks, as can be seen in Fig. 13.

In addition, it should be noted that the thickness of both the sintered Ag joint and the Pb5Sn solder joint in the present work are typical for those used in both die attachment technologies. The sintered Ag joint is less compliant than the Pb5Sn solder joint because the former is thinner and has relatively high Young's modulus [33], [34]. It is actually easier to increase the thickness of the sintered Ag joint than the Pb5Sn solder joint for increasing its compliance and reducing the stresses so as to further increase the power cycling reliability. Therefore, the present results are valid to compare the high lead solder joint with the sintered Ag joint formed under the specified sintering parameters.

V. Conclusion

The evolution of the thermal resistance and microstructures of low pressure nano-silver sintered joints were compared with high temperature Pb5Sn solder joints. The conclusions can be summarized as follows:

(1) When a failure criterion of a 20 % increase in the effective thermal resistance for the Pb5Sn solder joint was chosen, the sintered nano-silver joint has a lifetime at least 10 times longer when used to attach 13.5 mm $\times$ 13.5 mm power dies. In such a case, the Pb5Sn solder joint has a lifetime of 11k power cycles.

(2) The effective thermal resistance of the Pb5Sn solder joint degraded gradually from 0.0467 K/W to 0.133 K/W after 41k power cycles, and then experienced a dramatic increase with further cycles. The gradual increase in the thermal resistance can be related to the formation and growth of grain boundary sliding-induced creep cracks which are approximately inclined at 45° at the through thickness direction of the die attachment. The dramatic increase was caused by the emergence of interfacial cracks at the solder/Ni-Sn IMC interface at the substrate side.

(3) The effective thermal resistance value of the sintered Ag die attachment appeared to remain constant at 0.04 ± 0.004 W/K before 80k power cycles, and then increased slightly. This is thought to be due to continued, post-sintering densification of the Ag layer during power cycling, leading to a nominal reduction in the thermal resistance of the denser Ag layer, but with the formation and growth of vertical cracks causing a comparable increase in the effective thermal resistance. The slight increase in the effective thermal resistance after 80k power cycles can be related to delamination of the Ag from the Si die occurring locally at the relatively wide cracks.

(4) Under constant current power cycling conditions the mechanism of failure for the Pb5Sn solder joint was the formation and growth of grain boundary sliding-induced creep cracks. For the nano-silver sintered joint, the formation and growth of the vertical cracks can be attributed to further densification and development of tensile stress and strain within the sintered Ag layer. The extension of the vertical cracks into the upper copper layer of the substrate can also be related to the further densification and formation and subsequent growth of vertical cracks within the sintered die attachment layer.

Acknowledgment

The authors would like to thank O. Khaselev and M. Marczi of Alpha Assembly Solutions for providing nano-silver film.

References

[1] S. H. Mannan and M. P. Clode, "Materials and processes for implementing high-temperature liquid interconnects," *IEEE Trans. Adv. Packag.*, vol. 27, no. 3, pp. 508–514, Aug. 2004.

[2] P. O. Quintero and F. P. McCluskey, "Temperature cycling reliability of high-temperature lead-free die-attach technologies," *IEEE Trans. Device Mater. Rel.*, vol. 11, no. 4, pp. 531–539, Dec. 2011.

[3] S. Tabatabaei, A. Kumar, H. Ardebili, P. J. Loos, and P. M. Ajayan, "Synthesis of Au–Sn alloy nanoparticles for lead-free electronics with unique combination of low and high melting temperatures," *Microelectron. Rel.*, vol. 52, no. 11, pp. 2685–2689, 2012.

[4] H. A. Mustain, W. D. Brown, and S. S. Ang, "Transient liquid phase die attach for high-temperature silicon carbide power devices," *IEEE Trans. Compon. Packag. Technol.*, vol. 33, no. 3, pp. 563–570, Sep. 2010.
[5] S. W. Yoon, K. Shiozaki, S. Yasuda, and M. D. Glover, "Highly reliable nickel-tin transient liquid phase bonding technology for high temperature operational power electronics in electrified vehicles," in *Proc. 27th Annu. IEEE Appl. Power Electron. Conf. Expo. (APEC)*, Orlando, FL, USA, 2012, pp. 478–482.
[6] Z. Zhang and G.-Q. Lu, "Pressure-assisted low-temperature sintering of silver paste as an alternative die-attach solution to solder reflow," *IEEE Trans. Electron. Packag. Manuf.*, vol. 25, no. 4, pp. 279–283, Oct. 2002.
[7] H. Schwarzbauer, "Method of securing electronic components to a substrate," U.S. Patent 4 810 672, Mar. 7, 1989.
[8] C. Weber, M. Hutter, S. Schmitz, and K. D. Lang, "Dependency of the porosity and the layer thickness on the reliability of Ag sintered joints during active power cycling," in *Proc. IEEE 65th Electron. Compon. Technol. Conf. (ECTC)*, San Diego, CA, USA, 2015, pp. 1866–1873.
[9] E. Ide, S. Angata, A. Hirose, and K. F. Kobayashi, "Metal–metal bonding process using Ag metallo-organic nanoparticles," *Acta Materialia*, vol. 53, no. 8, pp. 2385–2393, 2005.
[10] J. G. Bai and G.-Q. Lu, "Thermomechanical reliability of low-temperature sintered silver die attached SiC power device assembly," *IEEE Trans. Device Mater. Rel.*, vol. 6, no. 3, pp. 436–441, Sep. 2006.
[11] Y. Akada *et al.*, "Interfacial bonding mechanism using silver metallo-organic nanoparticles to bulk metals and observation of sintering behavior," *Mater. Trans.*, vol. 49, no. 7, pp. 1537–1545, 2008.
[12] H. Zheng, J. Calata, K. Ngo, S. Luo, and G.-Q. Lu, "Low-pressure (<5 MPa) low-temperature joining of large-area chips on copper using nanosilver paste," in *Proc. 7th Int. Conf. Integr. Power Electron. Syst. (CIPS)*, 2012, pp. 1–6.
[13] A. A. Wereszczak, D. J. Vuono, L. Zhenxian, and E. E. Fox, "Sintered silver joint strength dependence on substrate topography and attachment pad geometry," in *Proc. 7th Int. Conf. Integr. Power Electron. Syst. (CIPS)*, Nuremberg, Germany, 2012, pp. 1–6.
[14] M. Knoerr and A. Schletz, "Power semiconductor joining through sintering of silver nanoparticles: Evaluation of influence of parameters time, temperature and pressure on density, strength and reliability," in *Proc. 6th Int. Conf. Integr. Power Electron. Syst. (CIPS)*, Nuremberg, Germany, 2010, pp. 1–6.
[15] C. Buttay *et al.*, "Die attach of power devices using silver sintering—Bonding process optimization and characterization," in *Proc. High Temperature Electron. Netw. (HiTEN)*, Oxford, U.K., 2011, pp. 1–7.
[16] S. Fu, Y. Mei, X. Li, P. Ning, and G.-Q. Lu, "Parametric study on pressureless sintering of nanosilver paste to bond large-area ($\geq$100 mm^2) power chips at low temperatures for electronic packaging," *J. Electron. Mater.*, vol. 44, no. 10, pp. 3973–3984, 2015.
[17] X. Li *et al.*, "High temperature ratcheting behavior of nano-silver paste sintered lap shear joint under cyclic shear force," *Microelectron. Rel.*, vol. 53, no. 1, pp. 174–181, 2013.
[18] D.-J. Yu, X. Chen, G. Chen, G.-Q. Lu, and Z.-Q. Wang, "Applying Anand model to low-temperature sintered nanoscale silver paste chip attachment," *Mater. Design*, vol. 30, no. 10, pp. 4574–4579, 2009.
[19] F. Le Henaff *et al.*, "A preliminary study on the thermal and mechanical performances of sintered nano-scale silver die-attach technology depending on the substrate metallization," *Microelectron. Rel.*, vol. 52, nos. 9–10, pp. 2321–2325, 2012.
[20] M. Hutter, C. Weber, C. Ehrhardt, and K.-D. Lang, "Comparison of different technologies for the die attach of power semiconductor devices conducting active power cycling," in *Proc. 9th Int. Conf. Integr. Power Electron. Syst. (CIPS)*, Nuremberg, Germany, 2016, pp. 1–7.
[21] L. A. Navarro *et al.*, "Thermomechanical assessment of die-attach materials for wide bandgap semiconductor devices and harsh environment applications," *IEEE Trans. Power Electron.*, vol. 29, no. 5, pp. 2261–2271, May 2014.
[22] K. Guth *et al.*, "New assembly and interconnect technologies for power modules," in *Proc. 7th Int. Conf. Integr. Power Electron. Syst. (CIPS)*, Nuremberg, Germany, 2012, pp. 1–5.
[23] M. Knoerr, S. Kraft, and A. Schletz, "Reliability assessment of sintered nano-silver die attachment for power semiconductors," in *Proc. 12th Electron. Packag. Technol. Conf. (EPTC)*, 2010, pp. 56–61.
[24] M. A. Eleffendi, L. Yang, P. Agyakwa, and C. M. Johnson, "Quantification of cracked area in thermal path of high-power multi-chip modules using transient thermal impedance measurement," *Microelectron. Rel.*, vol. 59, pp. 73–83, Apr. 2016.
[25] J. F. Li, C. M. Johnson, C. Buttay, W. Sabbah, and S. Azzopardi, "Bonding strength of multiple SiC die attachment prepared by sintering of Ag nanoparticles," *J. Mater. Process. Technol.*, vol. 215, pp. 299–308, Jan. 2015.
[26] V. Székely, "On the representation of infinite-length distributed RC one-ports," *IEEE Trans. Circuits Syst.*, vol. 38, no. 7, pp. 711–719, Jul. 1991.
[27] V. Székely, "A new evaluation method of thermal transient measurement results," *Microelectron. J.*, vol. 28, no. 3, pp. 277–292, 1997.
[28] S. Kraft, A. Schletz, and M. Mäerz, "Reliability of silver sintering on DBC and DBA substrates for power electronic applications," in *Proc. 7th Int. Conf. Integr. Power Electron. Syst. (CIPS)*, 2012, pp. 1–6.
[29] H. Huang *et al.*, "Thermal resistance analysis of high power LED module under power cycling test," in *Proc. 15th Int. Conf. Electron. Packag. Technol. (ICEPT)*, Chengdu, China, 2014, pp. 1446–1449.
[30] C. Gobl, "Sinter technology enhances power-module robustness," 2009. [Online]. Available: http://powerelectronics.com/power_semiconductors/igbts/sinter-technology-enhances-power-modules-20091001/
[31] A. I. Attarwala, J. K. Tien, G. Y. Masada, and G. Dody, "Confirmation of creep and fatigue damage in Pb/Sn solder joints," *J. Electron. Packag.*, vol. 114, no. 2, pp. 109–111, 1992.
[32] N. Heuck *et al.*, "Aging of new interconnect-technologies of power-modules during power-cycling," in *Proc. 8th Int. Conf. Integr. Power Syst. (CIPS)*, 2014, pp. 1–6.
[33] N. Heuck *et al.*, "Analysis and modeling of thermomechanically improved silver-sintered die-attach layers modified by additives," *IEEE Trans. Compon. Packag. Manuf. Technol.*, vol. 1, no. 11, pp. 1846–1855, Nov. 2011.
[34] R. Darveaux and K. Banerji, "Constitutive relations for tin-based solder joints," *IEEE Trans. Compon. Packag. Manuf. Technol.*, vol. 15, no. 6, pp. 1013–1024, Dec. 1992.

Jingru Dai, photograph and biography not available at the time of publication.

Jianfeng Li, photograph and biography not available at the time of publication.

Pearl Agyakwa, photograph and biography not available at the time of publication.

Martin Corfield, photograph and biography not available at the time of publication.

Christopher Mark Johnson, photograph and biography not available at the time of publication.